THE JOURNAL OF BIOLOGICAL CHEMISTRY
Vol. 273, No. 49, Issue of December 4, pp. 32697–32707, 1998

Printed in U.S.A.

ShK-Dap^{22}, a Potent Kv1.3-specific Immunosuppressive Polypeptide*

(Received for publication, May 20, 1998, and in revised form, June 18, 1998)

Katalin Kalman, Michael W. Pennington‡, Mark D. Lanigan§, Angela Nguyen, Heiko Rauer¶, Vladimir Mahnir‖, Kathy Paschetto, William R. Kem‖, Stephan Grissmer¶, George A. Gutman, Edward P. Christian**, Michael D. Cahalan, Raymond S. Norton§, and K. George Chandy‡‡**

*From the Departments of Physiology & Biophysics, and Microbiology and Molecular Genetics, University of California, Irvine, California 92697-4560, ‡Bachem Bioscience, Incorporated, King of Prussia, Pennsylvania 19406, §Biomolecular Research Institute, Parkville 3052, Victoria, Australia, the ‖Department of Pharmacology and Therapeutics, College of Medicine, University of Florida, Gainesville, Florida 32610, the **Department of Respiratory, Inflammatory and Neurological Disorders, Zeneca Pharmaceuticals, Wilmington, Delaware 19850, and the ¶Department of Applied Physiology, University of Ulm, 89081 Ulm, Germany*

The voltage-gated potassium channel in T lymphocytes, Kv1.3, is an important molecular target for immunosuppressive agents. A structurally defined polypeptide, ShK, from the sea anemone *Stichodactyla helianthus* inhibited Kv1.3 potently and also blocked Kv1.1, Kv1.4, and Kv1.6 at subnanomolar concentrations. Using mutant cycle analysis in conjunction with complementary mutagenesis of ShK and Kv1.3, and utilizing the structure of ShK, we determined a likely docking configuration for this peptide in the channel. Based upon this topological information, we replaced the critical Lys^{22} in ShK with the positively charged, non-natural amino acid diaminopropionic acid (ShK-Dap^{22}) and generated a highly selective and potent blocker of the T-lymphocyte channel. ShK-Dap^{22}, at subnanomolar concentrations, suppressed anti-CD3 induced human T-lymphocyte [^{3}H]thymidine incorporation *in vitro*. Toxicity with this mutant peptide was low in a rodent model, with a median paralytic dose of ~200 mg/kg body weight following intravenous administration. The overall structure of ShK-Dap^{22} in solution, as determined from NMR data, is similar to that of native ShK toxin, but there are some differences in the residues involved in potassium channel binding. Based on these results, we propose that ShK-Dap^{22} or a structural analogue may have use as an immunosuppressant for the prevention of graft rejection and for the treatment of autoimmune diseases.

Human T lymphocytes express a unique voltage-gated potassium (Kv)[1] channel encoded by the Kv1.3 gene (1). A homotetramer of Kv1.3 subunits forms the functional channel in T lymphocytes (1). Earlier studies showed that structurally dissimilar blockers of this channel suppressed mitogen-induced [^{3}H]thymidine incorporation and interleukin-2 production by T lymphocytes (1–3). More specific, high affinity blockers discovered in recent years have demonstrated convincingly that Kv1.3 blockers depolarize the T-cell membrane and attenuate the calcium signaling pathway that is vital for lymphocyte activation (1, 4–9). Although Kv1.3 is found in B lymphocytes, macrophages, osteoclasts, platelets, and the brain, only in T lymphocytes does Kv1.3 channel activity seem to dominate the membrane potential (1, 8). The critical role of Kv1.3 during T-cell activation, coupled with its functionally restricted tissue distribution, has stimulated a search for potent and selective Kv1.3 antagonists for potential use as immunosuppressants (*e.g.* see Refs. 8 and 9).

Many potent polypeptide inhibitors of Kv1.3 have been isolated from scorpion venom. These polypeptides adopt well defined conformations constrained by 3 or 4 disulfide bonds and bind with extremely high affinity to a shallow vestibule at the external entrance to the Kv1.3 pore (10, 11). The most selective of these, margatoxin (MgTX), suppresses T-lymphocyte activation *in vitro* and is immunosuppressive *in vivo* (9), suggesting the possibility of using MgTX as an injectable immunosuppressant. However, MgTX potently blocks the closely related Kv1.1 and Kv1.2 channels (12, 13), which are expressed in the brain, peripheral nerves, and heart (14), raising concerns about potential cardiac and neuronal toxic side effects. Extensive efforts are therefore ongoing to identify other more selective and potent peptide and non-peptide inhibitors of Kv1.3.

Recently, a 35-amino acid-residue polypeptide (ShK) from the sea anemone *Stichodactyla helianthus* was shown to block the Kv1.3 channel at low picomolar concentrations (15, 16). Like scorpion toxins, ShK has a well defined conformation constrained by three disulfide bonds, minimizing possible structural changes upon its binding to the channel. However, the structure of ShK is significantly different from those of scorpion toxins (17, 18). Using alanine-scanning mutagenesis, the channel-binding surfaces of ShK (15, 16) and its closely related homologue, BgK (19), have been determined. Despite differences in the scaffolds, the sea anemone and scorpion toxins share a conserved diad of residues that is essential for block of potassium channels (16, 19). This diad consists of a critical lysine (Lys^{27} in the scorpion toxins and Lys^{22} and Lys^{25} in ShK and BgK) and a neighboring aromatic residue (Tyr^{36} in ChTX, Tyr^{23} in ShK, Tyr^{26} in BgK) separated by ~7 Å (19). Lys^{27}, in scorpion toxins, couples with the tyrosine (Tyr^{400} in Kv1.3, Tyr^{445} in *Shaker*) in the potassium channel selectivity filter (11, 20). A better understanding of the interactions between ShK and the Kv1.3 channel may guide the design of specific ShK mutants with the potential to be used clinically as immunosuppressants. Here, we describe a mutant polypeptide that shows selectivity for Kv1.3, inhibits T-cell activation *in vitro*, and is minimally toxic *in vivo*.

* This study was supported by National Institutes of Health Joint Grant GM54221 (to W. R. K., R. S. N., M. W. P., and K. G. C.), Grant NS14609 (to M. D. C.), and Deutsche Forschungsgemeinschaft Grant Gr848/4-1 (to S. G.). The costs of publication of this article were defrayed in part by the payment of page charges. This article must therefore be hereby marked "*advertisement*" in accordance with 18 U.S.C. Section 1734 solely to indicate this fact.

‡‡ To whom correspondence should be addressed. Tel.: 949-824-2133; Fax: 949-824-3143; E-mail: gchandy@uci.edu.

[1] The abbreviations used are: Kv, voltage-gated K^+ channel; Dap, diaminopropionic acid; ChTX, charybdotoxin; MgTX, margatoxin; Fmoc, *N*-(9-fluorenyl)methoxycarbonyl; NOE, nuclear Overhauser enhancement; MNC, mononuclear cell; r.m.s., root mean square.

MATERIALS AND METHODS

Peptide Synthesis—Fmoc-amino acid derivatives were obtained from Bachem A.G. (CH-4416 Bubendorf, Switzerland). Solid-phase assembly was initiated with Fmoc-Cys(Trt)-2-chlorotrityl resin to minimize potential racemization of the C-terminal Cys residue (21). Automated stepwise assembly was carried out entirely on an ABI-431A peptide synthesizer (Applied Biosystems, Foster City, CA). Fmoc-Dap(*t*-butyloxycarbonyl) was substituted in place of Lys^{22} in the assembly of the polypeptide. The Dap^{22}-substituted polypeptide was cleaved and deprotected with reagent K (22) containing 5% triisopropylsilane. The ShK-Dap^{22} analogue was solubilized, oxidized, and purified by reverse phase-high pressure liquid chromatography using the same method described previously for other ShK analogues (15). High pressure liquid chromatography-pure fractions were pooled and lyophilized. The structure and purity of the peptides were confirmed by reverse phase-high pressure liquid chromatography, amino acid analysis, and electrospray ionization-mass spectroscopy analysis. All other ShK analogues were synthesized, purified, and characterized as reported previously (15, 16). Samples were weighed and adjusted to account for peptide content prior to bioassay.

Reagents—Cell lines stably expressing *mKv1.1*, *rKv1.2*, *mKv1.3*, *hKv1.5*, and *mKv3.1* (7, 12) were maintained in Dulbecco's modified Eagle's medium containing 10% fetal calf serum and G418 (1 mg/ml). Human IK_{Ca} channels were studied in activated human T cells as described previously (7). All the *mKv1.3* mutants and *mKv1.4* used in this study have been described previously (7, 10–12). Rat *Kv1.6* and *rKv3.4* were gifts from Dr. Olaf Pongs (ZMNH Hamburg, Germany). ^{125}I-ChTX was purchased from NEN Life Science Products. Fetal calf serum and L-glutamine, penicillin, and streptomycin were obtained from Life Technologies, Inc. Anti-CD3 monoclonal antibody was acquired from Biomeda Inc (Foster City, CA).

^{125}I-ChTX Binding Assay—Membranes were prepared from a cell line stably transfected with the *hKv1.3* channel. The membranes were suspended at 50 μg/ml in incubation buffer (5 mM NaCl, 5 mM KCl, 10 mM HEPES, 6 mM glucose, pH 8.4) in Falcon 96-well polystyrene plates. Peptides were added in triplicate to wells at various concentrations. Cold ShK, ShK-Dap^{22}, or MgTX was added to the membranes for 30 min; ^{125}I-ChTX (25 pM, 2200 Ci/mmol) was then added, and the reaction was allowed to proceed at 22 °C for a further 20 min. The reaction was stopped by harvesting the membranes onto Packard GF/C Unifilter 96-well filter plates and by washing twice rapidly with ice-cold wash buffer (200 mM NaCl, 20 mM HEPES, pH 8.0). The filter plates were dried overnight, scintillation mixture (Packard Microscint-20; Packard Bioscience, Meriden, CT) was added, and the plates were counted in a scintillation counter (Packard Top Count). Specific binding was determined by subtracting nonspecific binding (defined by 100 nM unlabeled ChTX) from total binding. This binding assay was protein dependent, saturable (B_{max} = 916 ± 37 fmol/mg protein), and of high affinity (K_d = 23 pM).

Mouse Acute Toxicity Determinations—Several doses of ShK or ShK-Dap^{22} were administered by intravenous tail vein injection into 15–20-g Swiss-Webster male mice. Loss of righting ability (paralysis) was assessed over a 4-h period.

Activation of Human T Cells by Anti-CD3 Antibody—Mononuclear cells (MNCs) were isolated over a Ficoll-Hypaque density gradient (Sigma). The isolated MNCs were incubated (37 °C, 5% CO_2) for ≤2 days in RPMI 1640 supplemented with 10% fetal calf serum, 1 mM L-glutamine, 100 units/ml penicillin, and 100 μg/ml streptomycin. The assay was conducted in a 96-well plate by first adding monoclonal anti-CD3 and various polypeptide concentrations to wells in triplicate. Anti-CD3 was titrated to dilutions that produced a 4–25-fold increase in [^{3}H]thymidine incorporation. MNCs were resuspended in fresh media and then added to wells at a final concentration of 0.3 × 10^6 cells/well (final volume 200 μl). For determination of background uptake, anti-CD3 was not added to six wells in each plate, and the average [^{3}H]thymidine uptake from these wells subtracted from wells containing anti-CD3. Plates were incubated for 48 h, and [^{3}H]thymidine was added during the last 6 h. The contents of the wells were harvested onto glass fiber filters (Packard GF/C unifilters) using a multi-well harvester, and cells were lysed with water. Filters were air-dried overnight. Scintillation mixture (Packard Microscint-20) was added, and [^{3}H]thymidine incorporation was measured by counting in a scintillation counter.

Mammalian Cells—Each construct was linearized with *Eco*RI and transcribed *in vitro* (8, 10, 11). cRNA was diluted with fluorescent fluorescein isothiocyanate-dye (0.5% fluorescein isothiocyanate-Dextran in 100 mM KCl; fluorescein-dextran M_r 10,000, Molecular Probes, or from Sigma, Deisenhofen, Germany) to a final concentration of 1 mg/ml. The cRNA/fluorescein isothiocyanate solution was filled into injection capillaries (Femtotips, Eppendorf, Germany), and rat basophilic leukemic cells, chosen because they lack endogenous Kv channels (23), were injected using an Eppendorf microinjection system (Micromanipulator 5171 and Transjector 5246), as described previously (7, 24). Fluorescent cells were visualized 2–6 h later, and electrical currents were measured using the patch-clamp method. Experiments were performed at room temperature (21–25 °C) (7). Cells measured in the whole cell configuration were normally bathed in mammalian Ringer solution containing (in mM) 160 NaCl, 4.5 KCl, 2 $CaCl_2$, 1 $MgCl_2$, 10 HEPES, adjusted to pH 7.4 with NaOH, with an osmolarity of 290–320 mosM. A simple syringe-driven perfusion system was used to exchange the bath solutions in the recording chamber. The internal pipette solution for Kv channel recordings contained (in mM) 134 potassium fluoride, 1 $CaCl_2$, 2 $MgCl_2$, 10 HEPES, 10 EGTA, adjusted to pH 7.2 (with KOH), with an osmolarity of 290–320 mosM. The internal pipette solution for the K_{Ca} channel recordings contained (in mM) 135 potassium aspartate, 2 $MgCl_2$, 10 HEPES, 10 EGTA, 8.7 $CaCl_2$, adjusted to pH 7.2 (with KOH), with an osmolarity of 290–320 mosM ($[Ca^{2+}]_{free}$ of 10^{-6} M). Series resistance compensation (80%) was used if the current exceeded 2 nA. Capacitative and leak currents were subtracted using the P/8 or P/10 procedure. The holding potential in all experiments was −80 mV.

Oocytes—cRNA was transcribed *in vitro* and injected into oocytes (*Xenopus laevis* purchased from NASCO, Fort Atkinson, WI) (10, 11). Potassium currents were measured at room temperature using the two-voltage clamp technique (10, 11), and data were analyzed using pClamp software (version 5.5.1, Axon Instruments, Burlingame, CA). Whole oocytes were held at −100 mV and depolarized to +40 mV over 500 ms; time between pulses was 30 s. Capacitative and leak currents were subtracted prior to analysis using the P/4 procedure. The dissociation constant was calculated assuming a 1:1 binding of toxin to Kv1.3 as described (10, 11).

Mutant Cycle Analysis—This method provides a simple way to evaluate the strength of interaction between any two pairs of protein residues (25). For each mutant cycle, we measured the potency (K_d) of ShK and each of its mutants on Kv1.3 and each of the channel mutants.

Three positively charged ShK residues, Lys^9, Arg^{11}, and Lys^{22}, were replaced individually by the neutral residues alanine (Ala) or norleucine (Nle). In the mutant cycle studies, the wild-type polypeptide was compared against the corresponding neutral polypeptide. In addition, we replaced Lys^{22} with the non-natural positively charged residues, diaminopropionic acid (Dap) or ornithine (Orn). These residues vary in their side chain lengths (Dap = 2.5 Å, Orn = 5.0 Å, Nle = 5.0 Å, Lys = 6.3 Å). The positively charged position-22 mutants (along with Lys^{22}) were treated as wild-type in the mutant cycle analysis and compared against the mutant polypeptide containing the neutral residue Nle^{22}.

Four residues of the Kv1.3 channel were selected for mutagenesis: His^{404}, Asp^{402}, Tyr^{400}, and Asp^{386}. His^{404} was replaced with the hydrophobic residue Val, and Asp^{386} was replaced with Lys. As substitutions at positions 400 and 402 result in nonfunctional channels, we generated dimeric constructs containing one wild-type subunit and one mutant subunit. The resulting tetramers would be composed of (Asn$^{402}{}_2$,Asp$^{402}{}_2$) and (Val$^{400}{}_2$,Tyr$^{400}{}_2$). All of these channel mutants and the dimeric constructs have been used previously in mapping studies with kaliotoxin (10, 11).

The mutant cycles for Kv1.3-His^{404} and various ShK residues are shown as follows: Kv1.3(His^{404} → Val^{404})-ShK(Arg^{11} → Ala^{11}), Kv1.3(His^{404} → Val^{404})-ShK(Lys^9 → Ala^9), Kv1.3(His^{404} → Val^{404})-ShK(Lys^{22} → Nle^{22}), Kv1.3(His^{404} → Val^{404})-ShK(Dap^{22} → Nle^{22}), and Kv1.3(His^{404} → Val^{404})-ShK(Orn^{22} → Nle^{22}).

Similar cycles were constructed to measure coupling interactions between Asp^{386} (Asp^{386} → Lys^{386}), Asp^{402} (Asp$^{402}{}_4$ → Asn$^{402}{}_2$,Asp$^{402}{}_2$), Tyr^{400} (Tyr$^{400}{}_4$ → Val$^{400}{}_2$,Tyr$^{400}{}_2$), and polypeptide positions 9, 11, and 22.

The change in coupling energy, ΔΔG, for a given pair of ShK-Kv1.3 residues and their mutants was calculated using the formula ΔΔG = kT*ln*Ω, where Ω is a dimensionless value given by the formula Ω = [K_d (Wt ShK-Wt Kv1.3) × K_d (mut ShK-mut Kv1.3)]/[K_d (mut ShK-Wt Kv1.3) × K_d (Wt ShK-mut Kv1.3)]. For Ω values <1 the inverse was taken (10, 11). Schreiber and Fersht (25) reported that ΔΔG values of ≥0.5 kcal·mol^{-1} (2σ error) correspond to an inter-residue distance of ≤5 Å, and higher ΔΔG values match shorter inter-residue distances. We used a ΔΔG value of >0.8 kcal·mol^{-1} as an indicator of a close interaction (≤5 Å) between a pair of peptide and channel residues. Although high ΔΔG values indicate tight interactions, residues that are physically close may be energetically "silent" and may not be detected by this method (26).

All of the peptide-mapping studies were performed on channels expressed in *Xenopus* oocytes, whereas the studies described in Fig. 1 were performed on channels expressed in mammalian cells. In general, there was good correspondence between the K_d values measured on channels expressed in mammalian cells and oocytes, although ShK-Dap^{22} was about 6-fold more potent in the oocyte system (K_d = 3.3 ± 1.9 pM, n = 12) compared with mammalian cells (see Fig. 1).

Structure Determination—Two-dimensional ^{1}H NMR spectra were recorded at 600 MHz on a ~2 mM solution of synthetic ShK-Dap^{22} in 90% H_2O, 10% ^2H_2O (v/v) or 100% ^2H_2O at pH 4.9 and 293 K, as described (17, 27), but with water suppression using the Watergate scheme and a 3–9-19 selective pulse (28). Spectra were also recorded at 278 K in an attempt to sharpen backbone amide resonances from Ser^2, Cys^3, Met^{21}, Dap^{22}, and Tyr^{23}. Chemical shifts for Dap resonances in the synthetic peptide GlyGlyDapGlyGly-OH were measured from one-dimensional and total correlation spectroscopy spectra at 293 and 298 K in 90% H_2O, 10% ^2H_2O at pH 5.0, using 2,2-dimethyl-2-silapentane-5-sulfonate as internal standard.

A figure (Fig. S1) included in the "Appendix" summarizes the sequential assignments, slowly exchanging amides, backbone coupling constants, and medium-range NOEs for ShK-Dap^{22}, together with a table of ^{1}H chemical shifts (Table SI). Methods for obtaining distance and angle restraints, generating structures in DYANA (29), and refining the structures by restrained simulated annealing and restrained energy minimization in X-PLOR (30) were as described previously (17, 27). The final NMR restraint list (from which values redundant with the covalent geometry had been eliminated by DYANA) consisted of 82 intra-residue, 82 sequential, 105 medium-range (|i-j|<5), and 74 long-range (|i-j|≥5) upper bound restraints, no lower bound restraints, and 30 backbone and 6 side chain dihedral angle restraints. Of the 50 CHARMM-minimized structures, the best 25 were chosen on the basis of their stereochemical energies (*i.e.* excluding the electrostatic term). Of these, the best 20 were chosen on the basis of their Ramachandran plots and the consistency of their secondary structures with the NMR restraints. These structures and the NMR restraints on which they were based have been deposited in the Protein Data Bank (31) (code 1bei). Structures were analyzed using Insight II (Molecular Simulations Inc., San Diego) and MOLMOL (32). Hydrogen bonds were identified in MOLMOL using a maximum C-N distance of 2.4 Å and a maximum deviation of 35° from linearity.

Model of Kv1.3 and ShK Docking—To create a model of the pore and vestibule of Kv1.3 (residues 380–410), we relied heavily on the recent crystal structure of the bacterial K channel, KcsA (33, 34), and on a molecular model of the *Shaker* channel (35). Residues Phe^{425}, Lys^{427}, Thr^{449}, Gly^{452}, Phe^{453}, and Trp^{454} from the *Shaker* model (35) were changed to the corresponding Kv1.3 residues Gly^{380}, Asn^{382}, His^{404}, Thr^{407}, Ile^{408}, and Gly^{409}, respectively, using Insight II. Modifications to the backbone and side chain dihedral angles were then made so that the local and global structure of the channel model better resembled the corresponding region of the KcsA channel (33). Following conjugate gradient minimization of the model using Discover (MSI), the closest-to-average ShK structure (17) was juxtaposed with the channel so as to preclude steric contact between the two. The backbone atoms (N, C^α, and C) of Kv1.3 were fixed in space during the simulation, whereas the backbone fold of ShK was maintained by 16 medium-range and 3 long-range distance constraints. Inter-molecular distance constraints were added to the peptide-channel complex in conjunction with a 50 kcal mol^{-1} force constant in Discover so as to reflect data from mutant cycle analyses (see "Results"), with Lys^{22} N^ζ (ShK) being kept within 5 Å of Tyr^{400} C^γ from each of the four Kv1.3 subunits and Arg^{11} C^ζ being kept within 5 Å of a single His^{404} $N^{\delta1}$. A lower limit of 6 Å was maintained between Arg^{11} C^ζ and Asp^{402} C^γ to restrict any interaction between these two residues, which show no coupling (see "Results"). The complex was energy minimized using 10,000 steps of conjugate-gradient minimization, and then a 250-ps molecular dynamics simulation was performed *in vacuo* at 300 K with a 1-fs time step, a distance-dependent dielectric, and a 15-Å non-bonded interaction cut-off. After equilibration of the complex, the conformation with the lowest van der Waals repulsive energy was chosen for further energy minimization, carried out as above.

RESULTS

ShK, a Potent Blocker of the Kv1.3 Channel in T Lymphocytes—The polypeptide ShK blocks *mKv1.3* currents with a K_d of 11 ± 1.4 pM (n = 4, mean ± S.E.; Fig. 1*A*, Table I) and with 1:1 stoichiometry (Fig. 1*B*). Similar results were obtained for block of Kv1.3 channels in human peripheral blood T cells (data not shown).

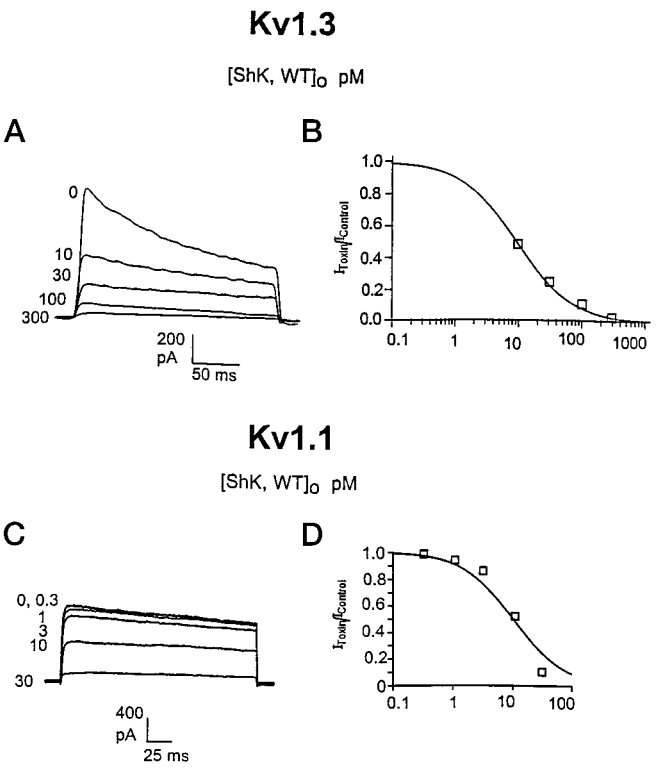

FIG. 1. **Electrophysiological analysis of ShK block of mKv1.3 and mKv1.1.** *A*, typical Kv1.3 currents expressed in rat basophilic leukemic cells or in a L929 cell line stably expressing these channels, studied in the whole cell configuration and blocked with ShK added to the external bathing solution. *B*, Hill plot of data in *A*. *C*, typical Kv1.1 currents in L929 cells studied in the whole cell configuration and blocked with external ShK. *D*, Hill plot of data in *C*.

TABLE I
Selectivity of ShK and ShK-Dap^{22} *on Kv channels*

IC_{50} in pM ± S.E.M.; number of determinations are shown in parentheses. The native intermediate conductance K_{Ca} channel in T lymphocyte was blocked with potency similar to the cloned *hKCa4* channel (data not shown).

Channel	ShK		ShK-Dap^{22}	
	pM			
mKv1.1	16 ± 3[b]	(3)	1,800 ± 577	(4)
rKv1.2	9,000 ± 300	(2)	39,000 ± 3200	(3)
mKv1.3	11 ± 1.4[b]	(4)	23 ± 3[b]	(4)
mKv1.4	312 ± 51[b]	(2)	37,000 ± 11,000	(2)
hKv1.5	>100,000	(3)	>100,000	(3)
hKv1.6	165 ± 3[b]	(2)	10,500 ± 900	(2)
mKv1.7	11,500 ± 2340	(3)	>100,000	(3)
mKv3.1	>100,000	(3)	>100,000	(3)
rKv3.4	>100,000	(3)	>100,000	(3)
hKCa4	28,000 ± 3,300	(3)	>100,000	(3)

The ShK polypeptide inhibited ^{125}I-ChTX binding to its receptor in the external vestibule of *hKv1.3*. Fig. 2 shows the concentration-dependent displacement of specifically bound ^{125}I-ChTX by ShK. Fitting the concentration-response curve to a Hill equation yields an IC_{50} value for ShK of 118 ± 20 pM (n = 5; mean ± S.E.) and 1:1 peptide:channel stoichiometry. Two ShK mutants, ShK-Dap^{22} and ShK-Nle^{22}, also displaced ^{125}I-ChTX binding to *hKv1.3* with 1:1 stoichiometry and IC_{50} values of 102 ± 17 pM (n = 8) and 663 ± 172 pM (n = 6), respectively. MgTX had an IC_{50} value of 78 ± 10 pM (n = 6) in the same binding assay. Collectively, the electrophysiology and binding data indicate that ShK and ShK-Dap^{22} are potent blockers of the Kv1.3 channel, and these sea anemone polypeptides inter-

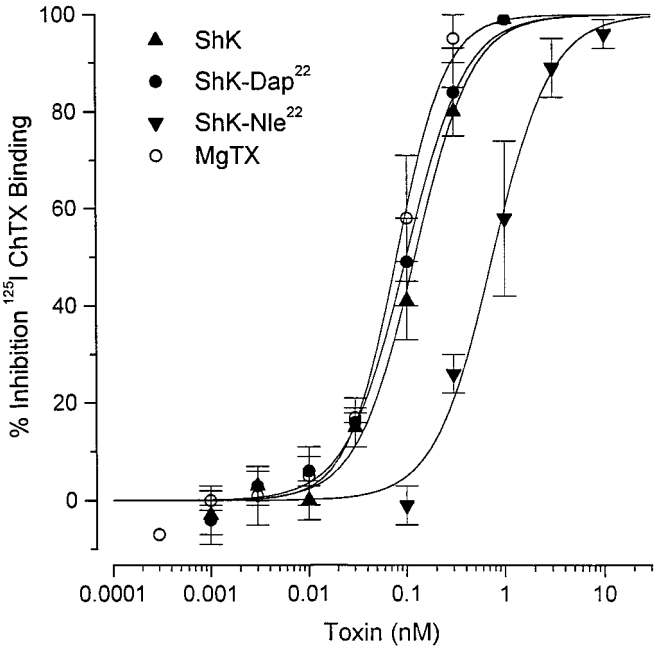

FIG. 2. **Peptide binding studies.** Points reveal the mean ± S.E. percent displacement (n = 4) by each peptide concentration of specifically bound ^{125}I-ChTX in membranes transfected with *hKv1.3*, as described under "Materials and Methods." Lines were iteratively fitted by Origin 4.1 software (Microcal Corp.) to the following expression: 100/[1+ (IC_{50}/x)^n], where x is toxin concentration, IC_{50} is the concentration producing one-half maximal block, and n is the Hill factor. Fitted parameters obtained from the individual experiments were ShK, IC_{50} 118 ± 20 pM, nH = 1.60 ± 0.18, n = 5; ShK-Dap^{22}, IC_{50} = 102 ± 17 pM, nH = 1.53 ± 0.15, n = 8; ShK-Nle^{22}, IC_{50} = 663 ± 172 pM, nH = 1.62 ± 0.27, n = 6; MgTX, IC_{50} = 79 ± 10 pM, nH = 1.71 ± 0.3, n = 6.

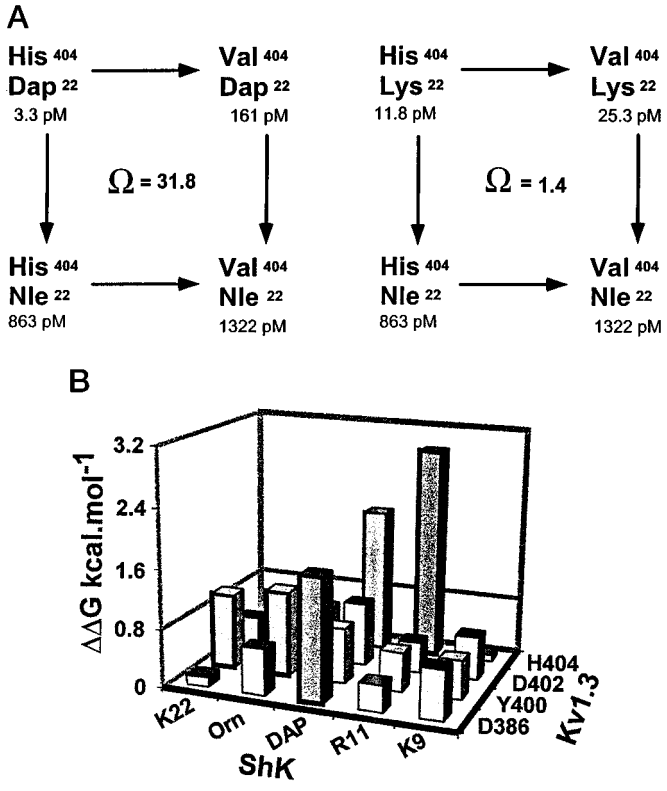

FIG. 3. **Identifying Kv1.3-peptide interactions by mutant cycle analysis.** *A*, mutant cycles for the pairs Kv1.3(His^{404} → Val^{404})-ShK-(Dap^{22} → Nle^{22}) and Kv1.3(His^{404} → Val^{404})-ShK(Lys^{22} → Nle^{22}). *B*, three-dimensional bar graph showing coupling energies ΔΔG (kcal·mol^{-1}) for various peptide-channel interactions. The *horizontal line* represents the 0.8 kcal·mol^{-1} cutoff (see "Materials and Methods"). Data for the mutant cycle Kv1.3(Asp^{386} → Lys^{386})-ShK(Arg^{29} → Ala^{29}) are as follows: Asp^{386}-Arg^{29}, K_d = 21 pM; Lys^{386}-Arg^{29}, K_d = 660 pM; Asp^{386}-Ala^{29}, K_d = 13 pM; Lys^{386}-Ala^{29}, K_d = 1920 pM; Ω = 4.7.

act with a receptor in the external vestibule of the Kv1.3 channel that is identical or overlapping the receptor surface for the scorpion toxins.

To evaluate the selectivity of ShK for Kv1.3, we tested it against a panel of eight K^+ channel targets (Table I). All the channels tested, with three exceptions, are >100-fold less sensitive to block by ShK compared with Kv1.3 (Table I). ShK, however, blocks *mKv1.1*, a cardiac and neuronal channel, with roughly the same potency as it does *mKv1.3* (Fig. 1, *C* and *D*), and two other channels, *mKv1.4* and *rKv1.6*, are also blocked in the picomolar range (Table I). Thus, ShK is not selective for Kv1.3, necessitating a search for an ShK mutant that might be more specific.

Identifying Polypeptide-Channel Interactions—Determination of the docking configuration of ShK in the Kv1.3 channel might help identify ShK mutants that exhibit Kv1.3 specificity. Guided by the solution structure of the ShK polypeptide (17) and by knowledge of the geometry of the pore and vestibule gained from studies with scorpion toxins (10, 11, 20), we generated complementary mutants of ShK and Kv1.3. Utilizing double mutant cycle analysis, we identified specific pairs of ShK-Kv1.3 interactions.

Three residues in ShK were chosen for mutagenesis: Arg^{11} and Lys^{22} on the surface, thought to interact with Kv1.3, and Lys^{9} on the opposite surface (15–18). We focused on four channel residues (His^{404}, Asp^{402}, Tyr^{400}, and Asp^{386}) that have been shown previously to be important for scorpion toxin binding (10, 11). His^{404} (KcsA-Tyr^{82}) lies at the outer entrance to the ion conduction pathway (10, 33). The ring of four His^{404} residues is unique to Kv1.3, and compounds that target this ring might be selective for the lymphocyte channel (1, 7, 8). The highly conserved Tyr^{400} (KcsA-Tyr^{78}) and Asp^{402} (KcsA-Asp^{80}) in the critical signature sequence (GYGD) form part of the ion selectivity filter and couple with Lys^{27} in the scorpion toxins (11, 20, 36). Asp^{386} (KcsA-Arg^{64}) lies ~10–14 Å from the center of the pore and interacts with Arg^{24} in kaliotoxin and agitoxin-2 and with Arg^{25} in charybdotoxin (10, 36).

Examples of two mutant cycles are presented in Fig. 3*A*. Replacing His^{404} in Kv1.3 with the hydrophobic valine (Val^{404}) significantly altered the interaction of ShK-Dap^{22} with the channel (ΔΔG = 2.0 kcal·mol^{-1}) but not that of the longer Lys^{22} analogue (ΔΔG = 0.19 kcal·mol^{-1}). Fig. 3*B* summarizes the results of mutant cycle experiments on several additional peptide-channel pairwise interactions. Collectively, these results identified seven pairs of significant ShK-Kv1.3 interactions involving four channel positions as follows: Arg^{11}-His^{404}, Lys^{22}-Tyr^{400}, Orn^{22}-Tyr^{400}, Orn^{22}-Asp^{402}, Dap^{22}-Asp^{402}, Dap^{22}-His^{404}, and Dap^{22}-Asp^{386}.

Using a molecular model of Kv1.3 based on the known crystal structure of the KcsA channel (33), we used restrained molecular dynamics simulations to dock the ShK peptide into the channel (Fig. 4). In this configuration, Lys^{22} protrudes into the pore, but its side chain does not make direct contact with the critical Tyr^{400} and Asp^{402} in Kv1.3 (Fig. 4); the corresponding residues in the KcsA channel face away from the channel pore (33). This docking configuration places Arg^{11} in close proximity to His^{404} in one channel subunit, and two of the remaining His^{404} residues in the tetramer lie in close proximity to peptide residues Met^{21} and Arg^{29}. In addition, our model places Arg^{29} near Asp^{386} in the channel subunit adjacent to that which interacts with Arg^{11}. Two lines of evidence support this placement. First, introduction of lysine at channel position 386 (D386K) causes a significant reduction in peptide potency

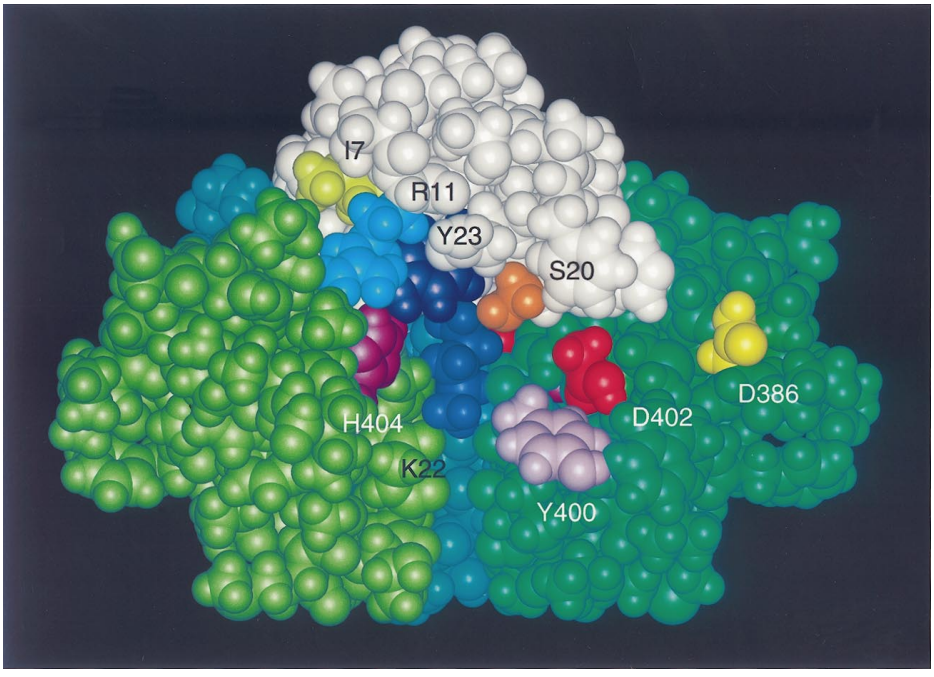

FIG. 4. **Side view of ShK (*white*) docked into the Kv1.3 model (*green*), with the channel subunit nearest the viewer removed.** Lys^{22} (*dark blue*) protrudes into the pore but does not make contact with Tyr^{400} (*pink*) from the channel. Other side chains are colored as follows: ShK Ile^{7}, *light green*; Arg^{11}, *cyan*; Ser^{20}, *orange*; Tyr^{23}, *purple*; Kv1.3 Asp^{386}, *yellow*; Asp^{402}, *red*; and His^{404}, *magenta*. In this view the side chains of Met^{21} and Phe^{27} of ShK are obscured by other residues. Note that the side chains of Asp^{386}, Asp^{402} and His^{404} of all three subunits are colored, but that the side chains visible in this view come from two different subunits. The channel subunits are shaded differently. This diagram was generated using Insight II.

(Kv1.3, 11.8 ± 4.8 pM, n = 11; Kv1.3 D386K, K_d = 563 ± 340 pM, n = 10), possibly via electrostatic repulsion of Arg^{29} on ShK. Second, we also detect coupling between Asp^{386} and Arg^{29} ($\Delta\Delta G$ = 0.88 kcal·mol^{-1}, Fig. 3 legend).

This docking configuration, which resembles that of agitoxin-2 docked in the KcsA channel (36), was used to guide the identification of ShK mutants that exhibit Kv1.3 specificity. For example, the ShK-Dap^{22} mutant that couples strongly with the ring of four His^{404} residues unique to Kv1.3 and makes contact with Asp^{386} might be selective for the lymphocyte channel. To test this idea, we evaluated the ShK-Dap^{22} mutant in our selectivity screen.

ShK-Dap^{22} Is a Potent and Selective Blocker of Kv1.3—The ShK-Dap^{22} mutant blocked *mKv1.3* currents with a K_d of 23 ± 3 pM (n = 4, mean ± S.E.; Fig. 5*A*) and a Hill coefficient close to unity (Fig. 5*B*). Human Kv1.3 channels are blocked with a similar potency (data not shown). ShK-Dap^{22} displaced ^{125}I-ChTX binding to *hKv1.3* with an IC_{50} of 102 ± 17 pM (n = 8; Fig. 2) and with 1:1 stoichiometry, indicating that the peptide binds in the external vestibule in a site overlapping the ChTX receptor. These results corroborate the mutant cycle data presented in Fig. 3.

In a selectivity screen, ShK-Dap^{22} was found to be a highly selective inhibitor of Kv1.3. ShK-Dap^{22} blocked *mKv1.1*, *mKv1.4*, *rKv1.6*, and other potassium channel targets with significantly less potency than Kv1.3 (Fig. 5, *C* and *D*; Table I).

ShK, ShK-Dap^{22}, and MgTX Inhibit Human T Cell Activation with Similar Potency—We compared the ability of ShK, ShK-Dap^{22}, and MgTX to suppress anti-CD3-stimulated [^{3}H]thymidine incorporation by human peripheral blood T cells. All three polypeptides inhibited mitogen-stimulated [^{3}H]thymidine incorporation to a maximum level of ~50–60% (Fig. 6). However, the midpoint of inhibition (IC_{50}) for each toxin was below 500 pM, in keeping with their affinity for the Kv1.3 channel. Consistent with our results, an earlier study reported that peripheral blood T cells isolated from mini-pigs during intravenous MgTX infusion never showed more than a ~60% inhibition of mitogen-stimulated [^{3}H]thymidine incorporation in an *ex vivo* proliferation assay (9).

ShK-Dap^{22} Does Not Exhibit Acute Toxicity following Intravenous Injection into Rodents—As an initial evaluation of the toxicity of ShK and ShK-Dap^{22}, mice (n = 5 in each case) were

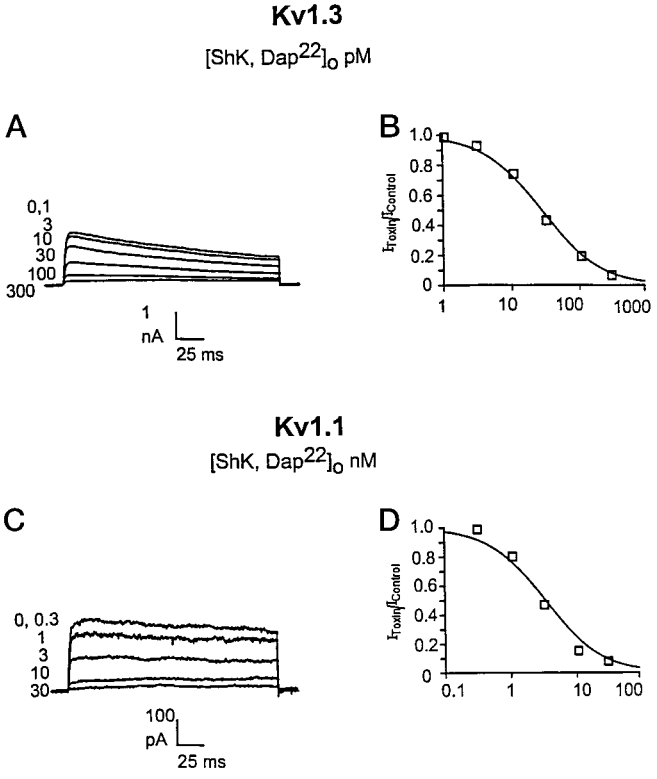

FIG. 5. *A*, typical Kv1.3 currents expressed in rat basophilic leukemic cells or in an L929 cell line stably expressing these channels, studied in the whole cell configuration and blocked with external ShK-Dap^{22}. *B*, Hill plot of data in *A*. *C*, external ShK-Dap^{22} is significantly less potent on Kv1.1. *D*, Hill plot of data in *C*.

injected intravenously with each polypeptide. ShK toxin displayed a remarkably low toxicity when injected into mice, the median paralytic dose being approximately 0.5 mg per 20 g mouse, or 25 mg/kg body weight. ShK-Dap^{22} was even less toxic; a 1.0-mg dose failed to cause any symptoms (hyperactivity or seizures) or mortality, and the median paralytic dose was ~200 mg/kg body weight.

Solution Structure of ShK-Dap^{22} and Comparison with the

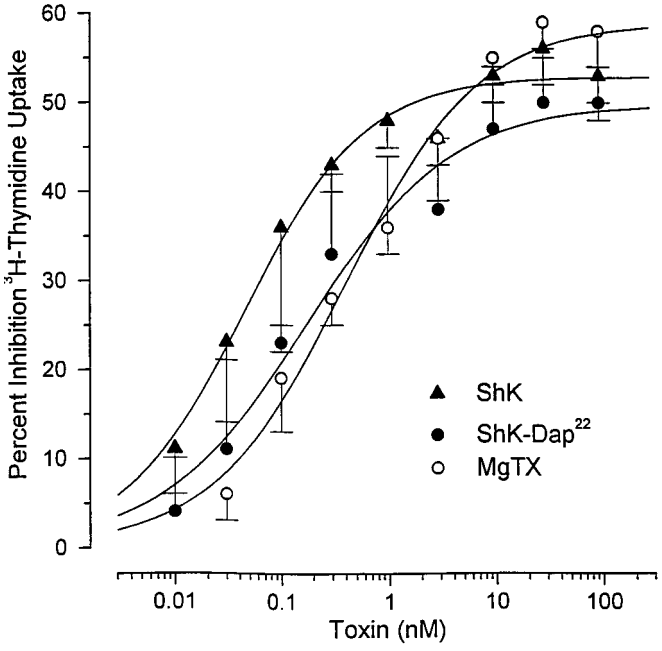

FIG. 6. **MgTX, ShK, and ShK-Dap^{22} suppress anti-CD3 induced [^{3}H]thymidine incorporation by human peripheral blood T cells.** *Points* show the mean percent (± S.E.; n = 4–10) inhibition produced by each peptide, as determined by the assay protocol described under "Materials and Methods." *Lines* were fitted iteratively by Origin to the following expression: $A_1/[1+ (IC_{50}/x)^n]$, where x is toxin concentration, A_1 is the maximal block achieved, IC_{50} is the concentration producing one-half maximal block, and n is the Hill factor for the fitted line. Fitted parameters obtained were as follows: ShK, A_1 = 53%, IC_{50} = 50 pM, nH = 0.77; ShK-Dap^{22}, A_1 = 50%, IC_{50} = 170 pM, nH = 0.64; MgTX, A_1 = 59%, IC_{50} = 390 pM, nH = 0.69.

Structure of Native ShK—Has replacement of Lys^{22} by Dap caused local conformational changes in the Kv1.3 binding surface of the polypeptide? Does ShK-Dap^{22} sit in Kv1.3 with a similar geometry as native ShK? To address these questions, we determined the solution structure of ShK-Dap^{22} using NMR data.

Structure of ShK-Dap^{22}—The structures are in good agreement with the experimental restraints and have good stereochemistry (Table II). Moreover, 91% of the residues have ϕ-ψ values in the generously allowed regions of a Ramachandran plot, Gly^{33} being the only residue with a positive ϕ angle. The angular order parameters (S) (37) of the final 20 structures indicate that residues 2–21 and 23–35 are well defined locally, with $S_{\phi,\psi} > 0.8$ (Fig. 7). Backbone r.m.s. difference values (Fig. 7*B*) also show that the structure is well defined over most of the molecule. Mean pairwise r.m.s. differences calculated over the backbone heavy atoms (N, C$^\alpha$, C) and all heavy atoms, respectively, of the whole molecule were 0.63 ± 0.15 and 1.41 ± 0.23 Å, and for the well defined region (residues 2–21 and 23–35) 0.51 ± 0.13 and 1.04 ± 0.14 Å.

The main secondary structure elements of ShK-Dap^{22} (Fig. 8, *A* and *B*) are two short α-helices encompassing residues 14–19 and 21–24. The N terminus adopts an extended conformation up to residue 8, where a pair of interlocking turns commences; in 25% of the structures this pair of turns satisfies the criteria for a 3_{10}-helix centered on residues 9–10 (with an 11→8 hydrogen bond found in all 20 structures). There is also a short stretch of helix between residues 29 and 32 (with a 32→28 hydrogen bond in all 20 structures) that is a mixture of α- and π-helix. Backbone hydrogen bonds associated with these secondary structural elements account for many of the slowly exchanging backbone amide protons observed by NMR following dissolution in ^2H_2O. Several other backbone amide protons found to be slowly exchanging were shielded from solvent.

TABLE II
Structural statistics for the 20 energy-minimized structures of ShK-Dap^{22} from X-PLOR

The best 20 structures after energy minimization in the distance geometry force field of X-PLOR were subsequently energy minimized in the CHARMM force field, using a distance-dependent dielectric. Values represent mean ± S.D.

r.m.s. deviations from experimental distance restraints (Å) (343)[a]		0.028 ± 0.001
r.m.s. deviations from experimental dihedral restraints (deg) (36)[a]		0.47 ± 0.15
r.m.s. deviations from idealized geometry		
Bonds (Å)		0.0107 ± 0.0006
Angles (deg)		2.66 ± 0.05
Impropers (deg)		0.37 ± 0.02
Energies (kcal·mol^{-1})		
E_{NOE}		14.1 ± 1.1
E_{cdih}		0.53 ± 0.28
E_{L-J}		−126 ± 7
$E_{bond} + E_{angle} + E_{improper}$		111 ± 4
E_{elec}		−513 ± 29
Mean pairwise r.m.s. difference (Å)		
Residues 1–35	0.63 ± 0.15[b]	1.41 ± 0.23[c]
Residues 2–21, 23–35	0.51 ± 0.13[b]	1.04 ± 0.14[c]

[a] The numbers of restraints are shown in parentheses. None of the structures had distance violations > 0.3 Å or dihedral angle violations > 5 °.
[b] Backbone heavy atoms.
[c] All heavy atoms.

Comparison with ShK—The overall structures of ShK and ShK-Dap^{22} are quite similar, as shown in Fig. 8*B*. Pairwise r.m.s. differences over the backbone heavy atoms N, C$^\alpha$, and C between the closest-to-average structures for ShK and ShK-Dap^{22} are 1.82 Å over residues 1–35, 1.70 Å over residues 2–21 and 23–35 (the well defined region of the analogue), and 1.38 Å over the well defined region of ShK (residues 3–33).

The main secondary structure elements of the two molecules are the same, but ShK-Dap^{22} also has a recognizable helix near the C terminus involving residues 29–32. In ShK, this region has a similar structure but does not satisfy the criteria for a helix. The only appreciable differences between the backbone dihedral angles of the two structures occur at Pro^8 (ψ), Thr^{31} (ϕ), and the three C-terminal residues (ϕ).

Potassium Channel Binding Residues in ShK-Dap^{22}—In Fig. 8*C*, the structures of ShK-Dap^{22} and ShK are aligned over N, C$^\alpha$, C, and C$^\beta$ of residues 11–23, which includes the most important residues for potassium channel binding (15, 16) (Figs. 3 and 4). In this view, the side chains of Arg^{11} and Tyr^{23} have similar orientations, although they have moved closer together. The distances from Tyr^{23} C$^\gamma$ to Arg^{11} C$^\gamma$ are 3.9 ± 0.2 and 7.4 ± 0.7 Å, respectively, in ShK-Dap^{22} and ShK. The functionally more important distances from the centroid and phenolic oxygen of Tyr^{23} to Arg^{11} C$^\zeta$ are, respectively, 4.9 ± 0.2 and 3.3 ± 0.2 Å in ShK-Dap^{22} and 6.7 ± 1.1 and 4.7 ± 1.4 Å in ShK. In ShK, the Lys^{22} side chain is not as well defined as other side chains in this region. The shorter Dap^{22} side chain of ShK-Dap^{22} is better defined and in most structures is oriented toward the Tyr^{23} ring (there may be a weak hydrogen-bonding interaction between the positively charged NH_3^+ group and the aromatic ring). Distances from the centroid and phenolic oxygen of Tyr^{23} to N$^\gamma$ or C$^\gamma$ of residue 22 are, respectively, 4.5 ± 1.1 and 4.9 ± 1.0 Å in ShK-Dap^{22} and 6.6 ± 0.8 and 8.1 ± 0.8 Å in ShK. Corresponding distances from C$^\zeta$ of Arg^{11} to N$^\gamma$ or C$^\gamma$ of residue 22 are, respectively, 8.0 ± 1.1 in ShK-Dap^{22} and 11.7 ± 1.5 Å in ShK. Thus, it seems that these three functionally important residues (11, 22, and 23) have moved closer together in ShK-Dap^{22}.

There has been an associated shift in the positions of the side chains of Ile^7 and Phe^{27}. The centroid of the aromatic ring of Tyr^{23} is 6.3 ± 0.2 Å from the centroid of the phenyl ring of Phe^{27} in ShK-Dap^{22}, compared with 4.5 ± 0.4 Å in ShK, and is

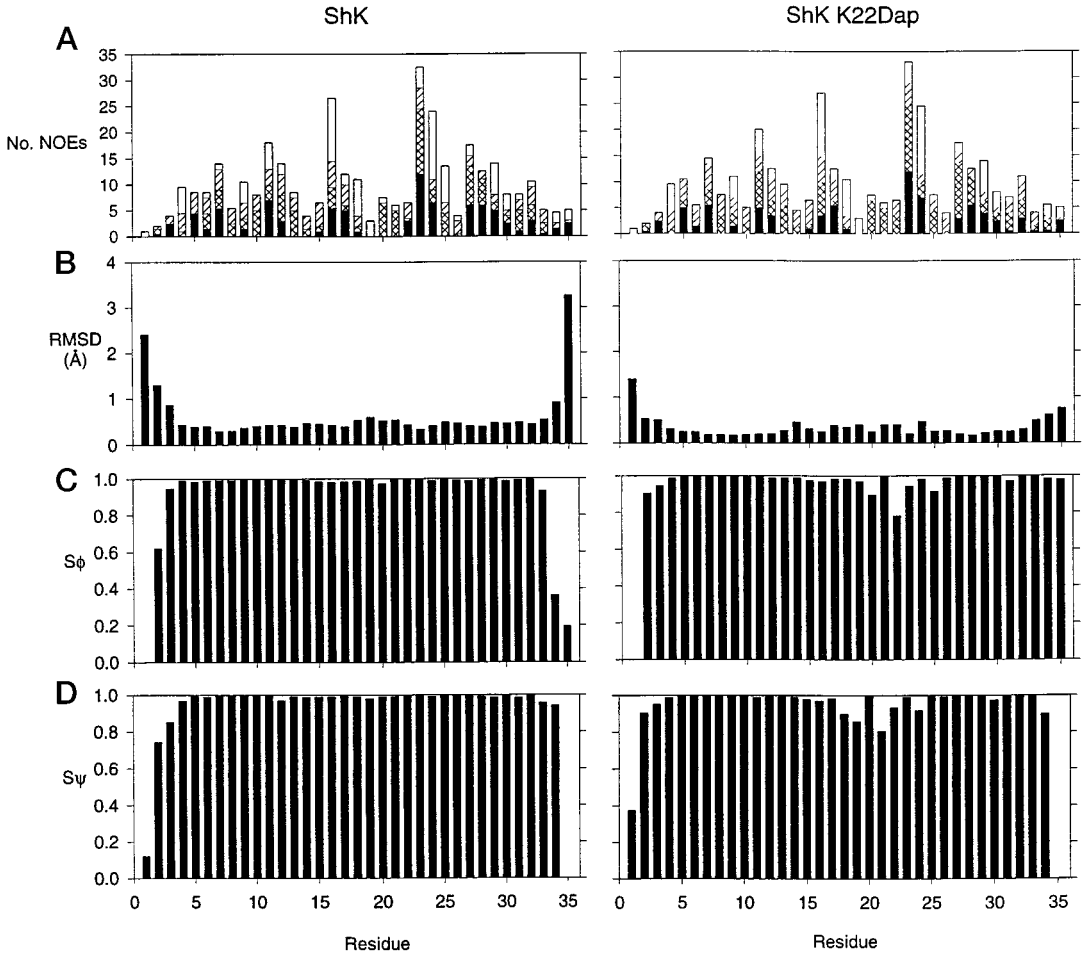

FIG. 7. **Parameters characterizing the final 20 structures of ShK-Dap^{22} plotted as a function of residue number.** Values for ShK (17) are shown on the *left side* for comparison. *A*, upper-bound restraints used in the final round of structural refinement shown as long-range (*black*), medium-range (*cross-hatched*), sequential (*diagonal shading*), and intra-residue (*unshaded*). *B*, r.m.s. differences from mean structure for N, C^{α}, and C atoms following superposition over the whole molecule. *C* and *D*, angular order parameters (*S*) for the backbone dihedral angles ϕ and ψ.

6.8 ± 0.2 Å from C^{β} of Ile^{7}, compared with 7.9 ± 0.7 Å in ShK. Distances from N^{γ} or C^{γ} of residue 22 to the centroid of the Phe^{27} ring, however, are unchanged at about 6.2 Å. The shorter side chain of Dap^{22} (compared with that of Lys^{22} in ShK) might be expected to increase the solvent accessibility of nearby residues. The largest increase in ShK-Dap^{22} (1.4-fold) was for His^{19}, with the flanking residues showing little deviation.

DISCUSSION

In this study, we pursued three overlapping goals. First, using the ShK peptide as a structural template and applying thermodynamic mutant cycle analysis, we determined the spatial proximity of eight pairs of ShK and Kv1.3 residues. These data, along with those obtained from earlier mapping studies with scorpion toxins (10, 11), guided our docking of ShK into the channel. This docking configuration might provide insights into the interaction of other members of this novel structural class of sea anemone peptides (*e.g.* BgK) and potassium channels. Second, we used the docking model to identify the Kv1.3-specific ShK mutant, ShK-Dap^{22}. ShK-Dap^{22} inhibited mitogen-stimulated human T-cell activation *in vitro* with subnanomolar potency and exhibited minimal toxicity *in vivo* in a rodent model. Third, we solved the structure of ShK-Dap^{22} by NMR. By comparing the structures of the native and mutant peptides, we attempted to understand the basis for the Kv1.3 specificity of ShK-Dap^{22}. These three complementary studies suggest that ShK-Dap^{22} might be a clinically useful immunosuppressant.

Peptide Toxins As Candidate Immunosuppressive Agents—The Kv1.3 channel is widely regarded as a novel therapeutic target for T-cell immunosuppression (*e.g.* Refs. 1, 8). Due to its restricted tissue distribution and unique role in regulating lymphocyte function, selective and potent blockers of this channel might not have the toxic side effects of currently used drugs such as cyclosporin, FK-506, and rapamycin (1, 8). Kv1.3-specific antagonists may therefore be therapeutically useful immunosuppressants.

Several scorpion toxins potently and reversibly block this channel with IC_{50} values in the low picomolar to nanomolar range and with 1:1 stoichiometry (10, 11). By blocking Kv1.3, these polypeptides attenuate the calcium signaling response and inhibit mitogen activation of T cells *in vitro* (4–9). The most potent and selective of these, MgTX, has also been shown to effectively suppress delayed-type hypersensitivity and alloimmune responses *in vivo* in micro- and mini-pigs, despite its inability to completely suppress T-lymphocyte activation *in vitro* (9). However, MgTX also potently blocks the closely related channels Kv1.1 and Kv1.2 (12, 13), which are expressed in the brain and peripheral neurons (14), and is therefore potentially toxic. An equally potent but more selective peptide blocker of Kv1.3 might not exhibit these side effects. The structurally defined peptidic inhibitor, ShK-Dap^{22}, exhibits the requisite potency and specificity for the Kv1.3 channel target.

Comparison of Structures of ShK and ShK-Dap^{22}—The overall structure of ShK-Dap^{22} is similar to that of native ShK toxin, but there are some differences in the side chains involved

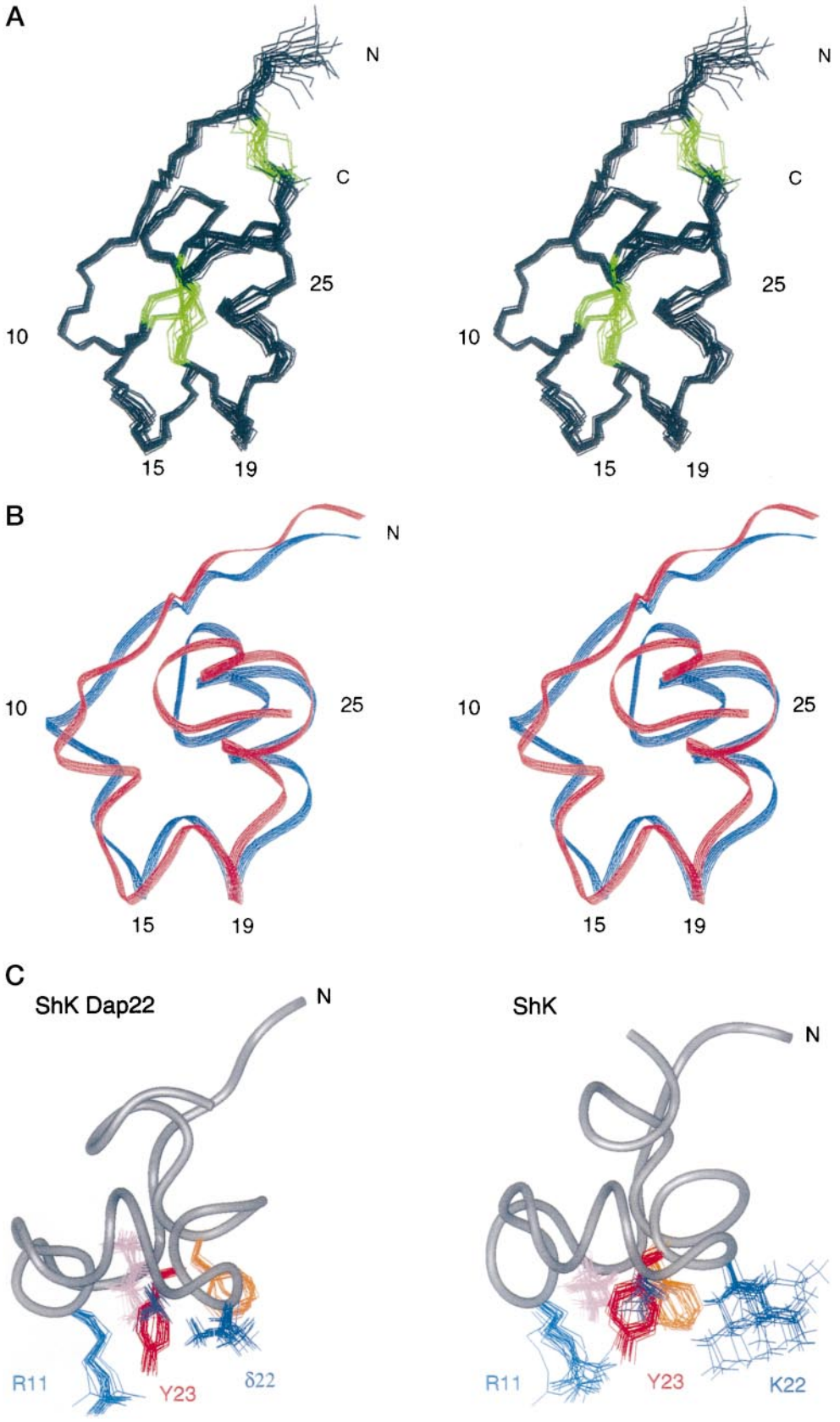

FIG. 8. **Solution structure of ShK-Dap^{22}.** *A*, stereo view of the best 20 structures of ShK-Dap^{22}, superimposed over the backbone heavy atoms N, C$^{\alpha}$, and C of residues 2–21 and 23–35. Only the backbone heavy atoms are shown, except for the three disulfide bonds (3–35, 12–28, and 17–32), which are shown in color. *B*, ribbon diagrams of the closest-to-average structures for ShK-Dap^{22} (*red*) and ShK (*blue*) superimposed over the backbone heavy atoms of residues 3–33, excluding residue 22. *C*, ribbon diagrams of ShK-Dap^{22} and ShK showing key residues for potassium channel binding (15, 16) as follows: Arg^{11} (*cyan*), Dap^{22}/Lys^{22} (*dark blue*), Tyr^{23} (*red*), Ile^{7} (*pink*), Ser^{20} (*purple*), and Phe^{27} (*orange*). The structures were aligned over N, C$^{\alpha}$, C, and C$^{\beta}$ of residues 11–23. The ribbon of the closest-to-average structure is shown in each case, together with the relevant side chains of all 20 structures. This diagram was generated using Insight II.

in Kv1.3 binding (Fig. 8). Are these differences significant, or do they reflect differences between the number and distribution of NMR-based restraints in key regions in the structure (Fig. 7*A*)? The ^{1}H chemical shifts of the two molecules are very similar, the only differences >0.1 ppm being for Met^{21} NH ($\Delta\delta$ 0.25 ppm), Dap^{22}, and residues 26–28 (Table SI and Fig. S2 in "Appendix"). The $^3J_{HNC\alpha H}$ coupling constants, which are dependent on backbone ϕ angles, also differed by >1Hz for residues 26, 27, and 29 (other residues in this category were 9, 10, 16, and 35). The backbone amide resonance of Dap^{22} was not observed, and those of Met^{21} and Tyr^{23} in ShK-Dap^{22} were broader than in ShK. As a result, there were fewer NOEs to these protons (Fig. S3 in "Appendix"), and this region of the structure is not as well defined in ShK-Dap^{22}. Part of the reason for the broader Dap^{22} NH resonance is that the intrinsic line width is greater, as found in the pentapeptide GlyGly-DapGlyGly; this presumably reflects the proximity of the side chain ammonium group of Dap to the backbone. However, this is unlikely to be the explanation for the flanking residues, suggesting that this region has greater conformational flexibility in ShK-Dap^{22}. To confirm the difference between ShK-Dap^{22} and ShK, we recorded a 2D NOE spectrum on a mixture of the two at pH 4.7 and 293 K. Resonance overlap prevented any comparison for Tyr^{23}, but it was quite clear that the cross-peaks from Met^{21} of ShK-Dap^{22} were broader and weaker than those of ShK. As the chemical shift of Met^{21} NH was also perturbed, it seems that there are some genuine differences in the local structure and dynamics of ShK-Dap^{22} around the substituted residue. The backbone amides of ShK-Dap^{22} also show slightly faster exchange than those of ShK (although respective rate constants are within a factor of 2), suggesting that the overall structure of ShK-Dap^{22} may be slightly more flexible than that of ShK.

In other regions, particularly the N and C termini, the apparent structural differences (Fig. 8) stem partly from the presence of a few NOEs unique to one of the restraint sets. The ShK-Dap^{22} structures are better defined than those of ShK at both termini, but it is important to note that there is some flexibility in these regions of both structures and that both may change when bound to Kv1.3. Finally, the close similarity between the structures of ShK-Dap^{22} and ShK confirms that the structure of this sea anemone toxin is different from that of the homologous BgK toxin (19) with which it shares 13 residues. BgK contains two longer helices, involving residues 9–16 and 24–31, although its overall topology is similar to that of ShK.

Why Does ShK-Dap^{22} Inhibit Kv1.1 Much Less Potently Than ShK?—The reasons for the specificity of ShK-Dap^{22} for Kv1.3 are not clear. It cannot be solely due to the interaction of Dap^{22} with the ring of unique His^{404} residues in Kv1.3, as replacement of these histidines with tyrosines (tyrosine is present at the equivalent position in Kv1.1) does not alter the peptide's affinity for Kv1.3 (K_d = 4.3 ± 2.5 pM, n = 3). A more likely explanation is that ShK-Dap^{22} sits slightly differently in the external vestibule of Kv1.3 compared with the native polypeptide. This notion is supported by our mutant cycle data, which show strong energetic contacts between Dap^{22} and both His^{404} and Asp^{386}. The lower affinity of Kv1.1 for ShK-Dap^{22} may be because of subtle differences in the architecture of the Kv1.1 and Kv1.3 vestibules that do not permit ShK-Dap^{22} to interact tightly with residues in the Kv1.1 vestibule. Without generating and evaluating several additional double mutants of Dap^{22} and other peptide positions, it is difficult to determine a precise docking configuration for ShK-Dap^{22} in the Kv1.3 and Kv1.1 vestibules. Further studies are underway to answer these questions.

Concluding Remarks—Although ShK-Dap^{22} has the potential to be used clinically, improving its stability and enhancing its plasma half-life are important objectives. Achievement of these goals would be facilitated by knowledge of the docking configuration of ShK-Dap^{22} in the Kv1.3 external vestibule. With this information, it might be possible to rationally substitute non-natural amino acids at key positions in the polypeptide, introduce stabilizers of the toxin's interactive surface, and generate a "minimal" analogue that retains the channel binding surface of full-length ShK-Dap^{22}. A smaller analogue might also increase the oral availability of the compound, thereby enhancing its therapeutic usefulness. In conclusion, we have described a highly potent and selective antagonist of Kv1.3 that might be used for the prevention of graft rejection and for the treatment of autoimmune diseases.

Acknowledgments—We are grateful to Kevin Barnham and Paul Pallaghy for helpful discussions and advice on the structure calculations, Raphael Röbe for performing some patch-clamp experiments, and Inna Zaydenberg, Michael E. Byrnes, David Behm, and Nancy Corrigan for help in peptide synthesis. We also appreciate excellent technical assistance of Christine Hanselmann, Luette Forrest, Katharina Ruff, Roseanna Khoury, Sue Rawa, and Dean Snyder. Finally, we thank Dr. Robert Guy for providing us with the *Shaker* model.

APPENDIX

TABLE SI
Proton chemical shifts of ShK-Dap^{22} at 20 °C and pH 4.9

Chemical shifts are in ppm and referenced to an impurity peak at 0.15 ppm. For methyl groups, two chemical shifts are listed where both protons could be assigned. Resonances assigned stereospecifically are underlined with the first entry having the lower branch number.

Residue	NH	αH	βH	γH	δH	Other
Arg^1	—[a]	4.10	1.95	1.69	3.23	N$^{\varepsilon}$H 7.30
Ser^2	8.92	4.48	3.80			
Cys^3	9.03	4.85	2.98			
Ile^4	7.78	4.66	1.95	C$^{\gamma}$H$_2$ 0.99, 1.19; C$^{\gamma}$H$_3$ 0.86;	0.81	
Asp^5	8.63	5.31	3.26, 2.70			
Thr^6	9.49	4.48	4.57	1.25		
Ile^7	7.27	4.79	1.90	C$^{\gamma}$H$_2$ 1.36, 0.85; C$^{\gamma}$H$_3$ 0.49;	0.53	
Pro^8	—	4.27	2.42, 1.76	1.95, 2.07	3.40, 3.82	
Lys^9	8.36	3.89	2.03, 1.86	1.52	1.75	C$^{\varepsilon}$H$_2$ 3.07
Ser^{10}	8.46	4.10	3.91			
Arg^{11}	8.15	4.44	1.94, 2.29	1.76	3.28, 3.14	N$^{\varepsilon}$H 7.47
Cys^{12}	7.99	5.04	3.28, 2.91			
Thr^{13}	7.28	4.38	4.78	1.31		O$^{\gamma}$H 5.84
Ala^{14}	8.88	3.98	1.47			
Phe^{15}	8.53	4.15	3.24, 2.88		C(2,6) 7.09;	C(3,5) 7.06 C(4) 6.86

TABLE SI—*continued*

Residue	NH	αH	βH	γH	δH	Other
Gln^{16}	7.80	4.18	1.95, 1.49		2.28, 2.35	$N^{\gamma}H_2$ 6.49, 6.47
Cys^{17}	8.52	4.22	3.20, 2.94			
Lys^{18}	7.52	4.01	1.57, 1.41	1.14	0.94	$C^{\epsilon}H_2$ 2.85
His^{19}	7.79	4.46	3.07, 2.35		C(4)H 6.50	C(2)H 8.34
Ser^{20}	8.35	5.05	4.10, 3.90			
Met^{21}	9.40	4.13	2.17, 2.67	2.56		$C^{\epsilon}H$ 2.06
Dap^{22}	—	4.19	3.09, 2.75	$N^{\gamma}CH_3^+$ 7.15		
Tyr^{23}	8.10	3.97	3.38, 2.61		C(2,6) 7.50;	C(3,5) 6.95
Arg^{24}	8.06	3.94	2.25, 1.77	1.70, 1.52	3.36, 3.22	$N^{\epsilon}H$ 7.37, $N^{\eta}H_2$ 6.51, 6.83
Leu^{25}	8.20	4.43	1.77, 1.49	1.68	0.89, 0.85	
Ser^{26}	7.21	4.74	3.55, 3.38			
Phe^{27}	7.48	5.30	3.27, 2.50		C(2,6) 6.20;	C(3,5) 7.22; C(4) 7.15
Cys^{28}	8.60	5.83	3.28, 3.13			
Arg^{29}	8.43	3.91	1.63, 1.83	1.46	3.27, 3.40	$N^{\epsilon}H$ 7.15, $N^{\eta}H_2$ 7.21, 6.64
Lys^{30}	7.21	4.17	1.84	1.32	1.63	$C^{\epsilon}H_2$ 3.09
Thr^{31}	10.87	3.87	4.08	1.32		
Cys^{32}	9.16	4.78	3.34, 2.91			
Gly^{33}	7.87	4.08, 4.08				
Thr^{34}	8.73	4.16	4.42	1.14		
Cys^{35}	7.79	4.33	3.34, 2.94			

[a] This resonance could not be assigned due to fast exchange with water.

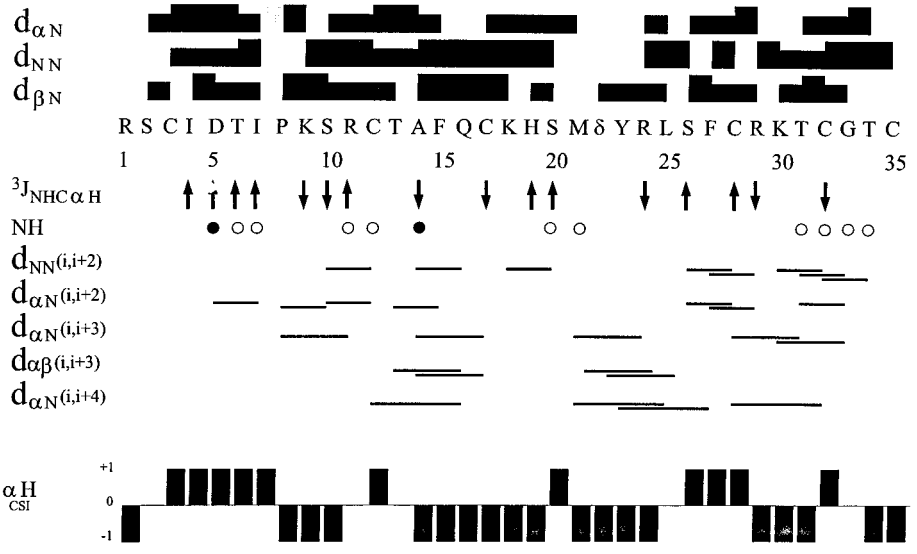

FIG. S1. **Summary of NOE connectivities and other NMR data for ShK-Dap^{22} at pH 4.9 and 293 K.** Dap^{22} is represented by δ. The intensities of $d_{\alpha N}$, d_{NN}, and $d_{\beta N}$ connectivities are represented as strong, medium, or weak by the height of the *bars*. The *shaded bar* indicates a $d_{\alpha\delta}$ connectivity to Pro^8. Medium range connectivities are also shown but with no indication of their relative strength. Values of $^3J_{NHC\alpha H} < 6$ Hz are indicated by ↓, those >8 Hz by ↑; blanks indicate values that could not be measured due to overlap or were between 6 and 8 Hz. Slowly exchanging amide protons (present up to 11.5 h after dissolution in ^2H_2O) are indicated by *filled circles* and those with intermediate exchange rates (present up to 6 h after dissolution in ^2H_2O) with *open circles*.

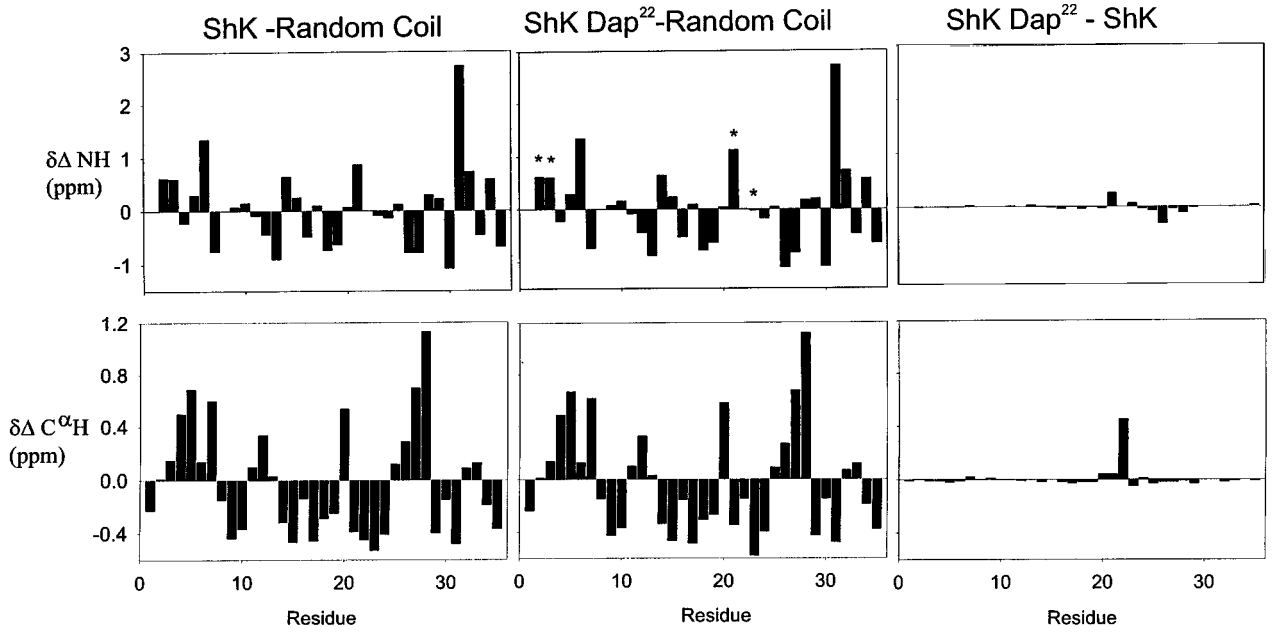

FIG. S2. **Plots of deviations from random coil chemical shifts (Δδ) (38) for NH and C$^{\alpha}$H resonances of ShK (*left*) and ShK-Dap^{22} (*center*).** Differences between the NH and C$^{\alpha}$H chemical shifts of ShK-Dap^{22} are shown on the *right*. *Asterisks* for ShK-Dap^{22} indicate NH resonances that were broad at 293 K compared with those of ShK.

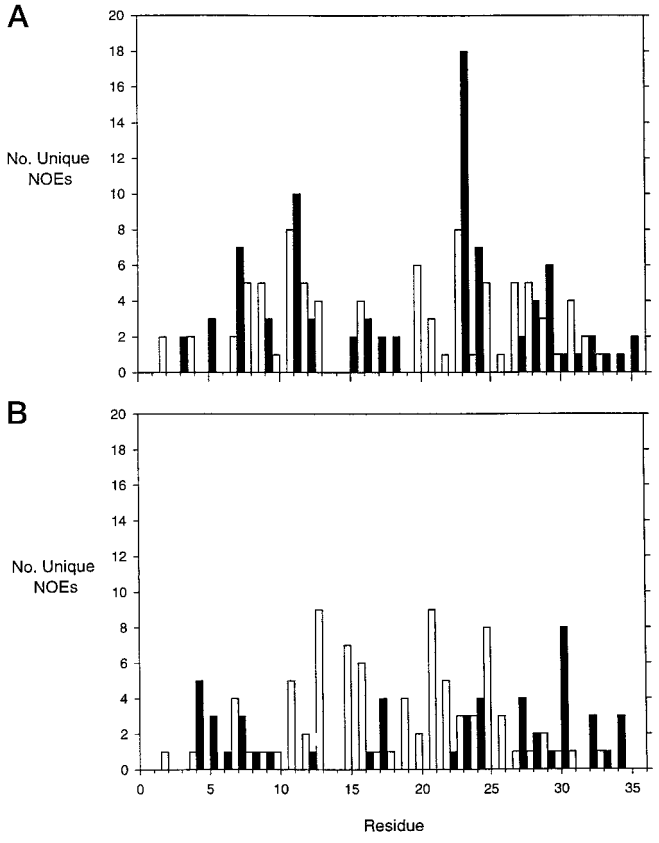

FIG. S3. **Unique medium and long range NOEs in ShK and ShK-Dap^{22} plotted as a function of residue number.** *Filled bars* indicate medium range NOEs, *open bars* long range NOEs. *A*, NOEs in ShK-Dap^{22} that were not present in native ShK; *B*, NOEs observed in ShK but not the analogue.

REFERENCES

1. Cahalan, M. D., and Chandy, K. G. (1997) *Curr. Opin. Biotechnol.* **8,** 749–756
2. DeCoursey, T. E., Chandy, K. G., Gupta, S., and Cahalan, M. D. (1984) *Nature* **307,** 465–468
3. Chandy, K. G., DeCoursey, T. E., Cahalan, M. D., McLaughlin, C., and Gupta, S. (1984) *J. Exp. Med.* **160,** 369–385
4. Price, M., Lee, S. C., and Deutsch, C. (1989) *Proc. Natl. Acad. Sci. U. S. A.* **86,** 10171–10175
5. Leonard, R. J., Garcia, M. L., Slaughter, R. S., and Reuben, J. P. (1992) *Proc. Natl. Acad. Sci. U. S. A.* **89,** 10094–10098
6. Lin, C. S., Boltz, R. C., Blake, J. T., Nguyen, M., Talento, A., Fischer, P. A., Springer, M. S., Sigal, N. H., Slaughter, R. S., Garcia, M. L., Kaczorowski, G. J., and Koo, G. C. (1993) *J. Exp. Med.* **177,** 637–645
7. Nguyen, A., Kath, J. C., Hanson, D. C., Biggers, M. S., Canniff, P. C., Donovan, C. B., Mather, R. J., Bruns, M. J., Rauer, H., Aiyar, J., Lepple-Wienhues, A., Gutman, G. A., Grissmer, S., Cahalan, M. D., and Chandy, K. G. (1996) *Mol. Pharmacol.* **50,** 1672–1679
8. Kath, J. C., Hanson, D. C., and Chandy, K. G. (1997) *Ann. Rep. Med. Chem.* **32,** 181–190
9. Koo, G. C., Blake, J. T., Talento, A., Nguyen, M., Lin, S., Sirotina, A., Shah, K., Mulvany, K., Hora, D., Cunningham, P., Wunderler, D. L., McManus, O. W., Slaughter, R., Bugianesi, R., Felix, J., Garcia, M., Williamson, J., Kaczorowski, G., Sigal, N. H., Springer, M. S., and Feeney, W. (1997) *J. Immunol.* **158,** 5120–5128
10. Aiyar, J., Withka, J. M., Rizzi, J. P., Singleton, D. H., Andrews, G. C., Lin, W., Boyd, J., Hanson, D. C., Simon, M., Dethlefs, B., Lee, C-L., Hall, J. E., Gutman, G. A., and Chandy, K. G. (1995) *Neuron* **15,** 1169–1181
11. Aiyar, J., Rizzi, J. P., Gutman, G. A., and Chandy, K. G. (1996) *J. Biol. Chem.* **271,** 31013–31016
12. Grissmer, S., Nguyen, A. N., Aiyar, J., Hanson, D. C., Mather, R. J., Gutman, G. A., Karmilowicz, M. J., Auperin, D. D., and Chandy, K. G. (1994) *Mol. Pharmacol.* **45,** 1227–1234
13. Koch, R. O., Wanner, S. G., Koschak, A., Hanner, M., Schwarzer, C., Kaczorowski, G, J., Slaughter, R. S., Garcia, M. L., and Knaus H-G. (1997) *J. Biol. Chem.* **272,** 27577–27581
14. Chandy, K. G., and Gutman, G. A. (1995) in *Handbook of Receptors and Channels: Ligand- and Voltage-gated Ion Channels* (North, R. A., ed) pp. 1–71, CRC Press, Inc., Boca Raton, FL
15. Pennington, M. W., Mahnir, V. M., Krafte, D. S., Zaydenberg, I., Byrnes, M. E., Khaytin, I., Crowley, K., and Kem, W. R. (1996) *Biochem. Biophys. Res. Commun.* **219,** 696–701
16. Pennington, M. W., Mahnir, V. M., Krafte, D. S., Khaytin, I., Zaydenberg, I., Byrnes, M. E., and Kem, W. R. (1996) *Biochemistry* **35,** 16407–16411
17. Tudor, J. E., Pallaghy, P. K., Pennington, M. W., and Norton, R. S. (1996) *Nat. Struct. Biol.* **3,** 317–320
18. Tudor, J. E., Pennington, M. W., and Norton, R. S. (1998) *Eur. J. Biochem.* **251,** 133–141
19. Dauplais, M., Leqoc, A., Song, J., Cotton, J., Jamin, N., Gilquin, B., Roumestand, C., Vita, C., de Medeiros, C. L. C., Rowan, E. G., Harvey, A. L., and Menez, A. (1997) *J. Biol. Chem.* **272,** 4302–4309
20. Ranganathan, R., Lewis, J. H., and MacKinnon, R. (1996) *Neuron* **16,** 131–139
21. Fujiwara, Y., Akaji, K., and Kiso, Y. (1994) *Chem. Pharm. Bull.* **42,** 724–726
22. King, D. S., Fields, C. G., and Fields, G. (1990) *Int. J. Peptide Protein Res.* **6,** 255–266
23. McCloskey, M., and Cahalan, M. D. (1990) *J. Gen. Physiol.* **95,** 208–222
24. Ikeda, S. R., Soler, F., Zuhlke, R. D., Joho, R. H., and Lewis, D. L. (1992) *Pflugers Arch.* **422,** 210–203
25. Schreiber, G., and Fersht, A. R. (1995) *J. Mol. Biol.* **248,** 478–486
26. Clackson T., and Wells, J. A. (1995) *Science* **267,** 383–386
27. Pallaghy, P. K., Alewood, D., Alewood, P. F., and Norton, R. S. (1997) *FEBS Lett.* **419,** 191–196
28. Sklenar, V., Piotto, M., Leppik, R., and Saudek, V. (1993) *J. Magn. Reson. Series A* **102,** 241–245
29. Güntert, P., Mumenthaler, C., and Wüthrich, K. (1997) *J. Mol. Biol.* **273,** 283–298
30. Brünger, A. T. (1992) *X-PLOR Version 3.1.* A System for X-ray Crystallography and NMR. Yale University, New Haven, CT
31. Bernstein, F. C., Koetzle, T. F., Williams, G. J. B., Meyer, E. F., Brice, M. D., Rodgers, J. R., Kennard, O., Shimanouchi, T., and Tasumi, M. (1977) *J. Mol. Biol.* **112,** 535–542
32. Koradi, R., Billeter, M., and Wüthrich, K. (1996) *J. Mol. Graphics* **14,** 51–55
33. Doyle, D. A., Cabral, J. M., Pfuetzner, R. A., Kuo, A., Gulbis, J. M., Cohen, S. L., Chait, B. T., and MacKinnon, R. (1998) *Science* **280,** 69–77
34. Li, H. L., Sui, H. X., Ghanshani, S., Lee, S., Walian, P. J., Wu, C. L., Chandy, K. G., and Jap, B. K. (1998) *J. Mol. Biol.* **282,** 211–216
35. Durell, S. R., Hao, Y., and Guy, H. R. (1998) *J. Struct. Biol.* **121,** 263–284
36. MacKinnon, R., Cohen, S. L., Kuo, A., Lee, A., and Chait, B. T. (1998) *Science* **280,** 106–109
37. Pallaghy, P. K., Duggan, B. M., Pennington, M. W., and Norton, R. S. (1993) *J. Mol. Biol.* **234,** 405–420
38. Wishart, D. S., Bigam, C. G., Holm, A., Hodges, R. S., and Sykes, B. D. (1995) *J. Biomol. NMR* **5,** 67–81

ShK-Dap^{22}, a Potent Kv1.3-specific Immunosuppressive Polypeptide

Katalin Kalman, Michael W. Pennington, Mark D. Lanigan, Angela Nguyen, Heiko Rauer, Vladimir Mahnir, Kathy Paschetto, William R. Kem, Stephan Grissmer, George A. Gutman, Edward P. Christian, Michael D. Cahalan, Raymond S. Norton and K. George Chandy

J. Biol. Chem. 1998, 273:32697-32707.
doi: 10.1074/jbc.273.49.32697
